JACS
JOURNAL OF THE AMERICAN CHEMICAL SOCIETY
Article
Cite This: J. Am. Chem. Soc. 2019, 141, 15684−15692
pubs.acs.org/JACS

Operando Characterization of Iron Phthalocyanine Deactivation during Oxygen Reduction Reaction Using Electrochemical Tip-Enhanced Raman Spectroscopy

Zhu Chen,[†] Song Jiang,[†] Gyeongwon Kang,[†] Duc Nguyen,[†] George C. Schatz,*[,†] and Richard P. Van Duyne*[,†,‡]

[†]Department of Chemistry and [‡]Applied Physics Graduate Program, Northwestern University, Evanston, Illinois 60208, United States

Supporting Information

ABSTRACT: Electrochemical tip-enhanced Raman spectroscopy (EC-TERS) has been implemented to investigate the structure and activity of iron(II) phthalocyanine (FePc)—a model catalyst for the oxygen reduction reaction (ORR). Using EC-TERS, both reversible change and irreversible degradation to FePc have been observed during ORR. The reversible change in the Raman spectrum of FePc can be related to the FePc molecules that adapt a nonplanar geometry during catalysis. In contrast, the irreversible degradation of FePc is a consequence of FePc demetalation, leading to the subsequent formation of free base phthalocyanine. This observation affirms that FePc demetalation during ORR proceeds via a direct loss of Fe^{2+} and that carbon corrosion is not the operative mechanism. Importantly, the FePc demetalation process can be correlated with a loss of ORR activity suggesting that Fe-containing sites are essential for FePc to achieve high catalytic activity. This study establishes EC-TERS as a promising technique for the operando characterization of electrocatalytic reactions at the molecular scale.

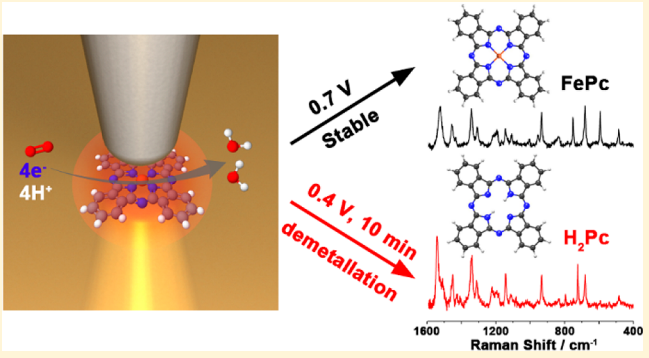

INTRODUCTION

A major drawback to the current polymer electrolyte fuel cells (PEFCs) is the high loading of expensive Pt-based catalysts, which are required to improve the sluggish kinetics associated with the oxygen reduction reaction (ORR).[1−3] Consequently, the development of active, stable, and affordable non-precious metal catalysts (NPMCs) has become a major focus in PEFC research. Among the alternatives to Pt-based catalysts, iron−nitrogen-containing carbon materials (Fe/N/C) are especially promising due to their excellent activity and low cost.[4−9] In spite of significant activity improvements to the Fe/N/C catalysts, important debates regarding the active site structure[6,7,9−17] and catalyst deactivation[18−29] remain ongoing.

Recently, significant efforts have been devoted to in situ characterizations of Fe/N/C catalysts under realistic operation conditions using techniques such as X-ray absorption spectroscopy,[6,11,14,30] Mössbauer spectroscopy,[13,22,31] and differential electrochemical mass spectrometry.[25] These empirical results combined with theoretical calculations[32,33] have led to the current inference that the pyridinic nitrogen coordinated Fe center(s)—FeN_x—in a graphitic network is critical for ORR. While there is strong evidence supporting the direct role of FeN_x as the active site, some studies have advocated that FeC[16] or CN_x[7,15,17] moieties are responsible for the ORR activity of Fe/N/C catalysts. Further impeding catalyst developments are the lack of understanding of catalyst deactivation. The proposed mechanisms for Fe/N/C deactivation hitherto involve either the loss of Fe via the demetalation of FeN_x sites[18−24,29] or the destruction of CN_x sites through carbon corrosion,[21−23,25−27] and there is ample evidence that supports both hypotheses.

While existing operando/in situ studies have contributed significantly toward understanding Fe/N/C catalysts, many of these techniques lack surface sensitivity, have low chemical contrast, and are unable to resolve nanoscale features. In this context, tip-enhanced Raman spectroscopy (TERS), which combines scanning probe microscopy and Raman spectroscopy, is an excellent probe for catalytic reactions.[34−36] This technique offers high surface and chemical sensitivities, excellent spatial resolution, and the ability to operate in electrochemical conditions.[36−38] TERS has been implemented in ultrahigh vacuum, ambient, and liquid conditions. Subnanometer chemical resolution of self-assembled molecules has been demonstrated using TERS under UHV conditions.[39−41] In addition, new catalytic insights were revealed regarding the activation of oxygen on cobalt phthalocyanine using TERS in UHV conditions in our recent study.[42] The

Received: July 25, 2019
Published: September 10, 2019

DOI: 10.1021/jacs.9b07979
J. Am. Chem. Soc. 2019, 141, 15684−15692

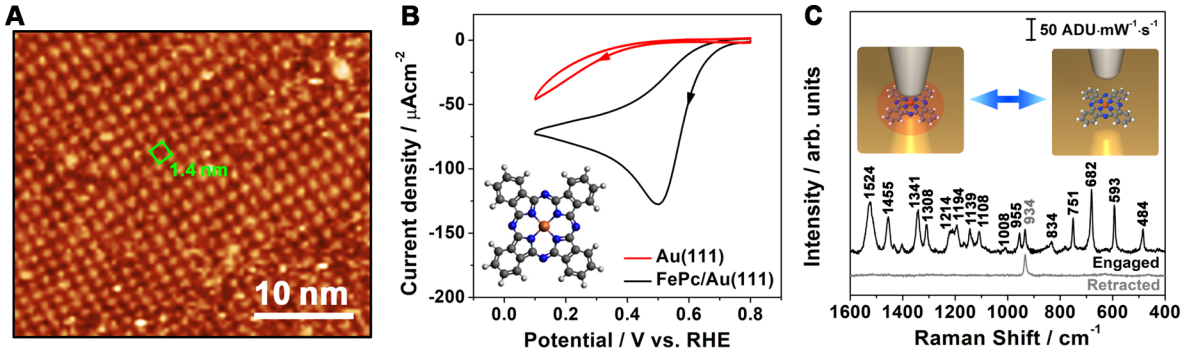

Figure 1. (A) EC-STM image of FePc/Au(111) at 0.7 V in 0.1 M $HClO_4$ acquired using a W tip. Imaging conditions: V_{bias} = 0.9 V, I_{tip} = 1.5 nA. (B) CV of FePc/Au(111) and Au(111) in aerated 0.1 M $HClO_4$ acquired at 50 mVs^{-1}. (C) Tip-engaged and tip-retracted EC-TER spectra of FePc/Au(111) at 0.7 V in 0.1 M $HClO_4$. TERS conditions: Ag tip, λ = 632.8 nm at 0.5 mW, V_{bias} = 0.3 V with I_{tip} = 0.5 nA, and 10 s integration time.

TERS technique has also been implemented to investigate chemical reactions,[43−45] surface chemistry,[46] localized strain,[47] and nanodefects[48] in ambient conditions. Continued progress in TERS has led to its application in electrochemistry, revealing nanoscale redox behavior and potential induced molecular reorientation.[37,49−55] These exemplary studies highlight the potential of TERS as a nanoscale probe for studying electrocatalysts during chemical reactions. In our recent studies, we have employed the TERS technique to characterize and manipulate cobalt phthalocyanine (CoPc), an active catalyst for the electrochemical synthesis of hydrogen peroxide.[52,54] Based on the change in the TERS intensity as a function of tip−sample bias, applied potentials, and excitation wavelengths, the dominant chemical state of CoPc during catalysis and the threshold bias required for CoPc manipulation were identified.[52,54]

Herein, we implement electrochemical TERS (EC-TERS) to monitor the chemical change and degradation of Fe(II) phthalocyanine (FePc) during ORR. FePc is selected as a model catalyst for this study based on its structural similarities compared to the proposed FeN_x active sites[6,9,11,24] and the ability to promote the four-electron reduction of oxygen with high efficiency.[18,24,56−58] Using EC-TERS, we present clear evidence of a reversible chemical change to FePc followed by an irreversible degradation during ORR catalysis. For the first time, we provide unambiguous evidence that supports phthalocyanine (H_2Pc) as the primary degradation product of FePc during ORR and that carbon corrosion is not the dominant mechanism for catalyst deactivation. Furthermore, FePc demetalation can be correlated with a decrease in the ORR activity, which supports the direct involvement of the FeN_4 moiety in catalysis.

EXPERIMENTAL SECTION

Sample Preparation for EC-TERS. An Au(111) single crystal (Princeton Scientific Corporation, 99.999%) was chemically cleaned in a piranha solution (1:3 volume mixture of H_2O_2 and H_2SO_4) for 30 min, followed by rinsing with a copious amount of Milli-Q water and immersing in ethanol (Aldrich, >99.5%) for 20 min. After chemical cleaning, the Au(111) single crystal was flame-annealed and cooled down in air. The flame-annealed Au(111) was transferred into a UHV system, and FePc molecules (Aldrich, 95%) were thermally evaporated onto the surface to form FePc/Au(111). The H_2Pc/Au(111) sample was prepared by incubating the flame-annealed Au(111) crystal in a H_2Pc-saturated benzene solution for 5 min.

Electrochemical Characterization of FePc/Au(111). The ORR activity of FePc/Au(111) was evaluated in an open electrochemical cell in 0.1 M $HClO_4$ (Aldrich, 99.999% metal basis). A schematic of the home-built electrochemical apparatus is given in the Supporting Information (Figure S1), and prior variants of the cell design were described by Ren et al.[37] and Domke et al.[51] The reference and counter electrodes used were silver (Ag, 99.99%, Alfa Aesar) and platinum wires (Pt, 99.99%, Alfa Aesar), respectively. A potentiostat (EC301, Stanford Research Systems) was used to establish voltage control for the electrochemical experiments. Hereafter, potential values are referenced to the reversible hydrogen electrode (RHE) unless stated otherwise. A conversion between the Ag pseudo reference electrode and the RHE scale is included in the Supporting Information (Figure S2). Cyclic voltammetry was performed by sweeping the sample potential from 0.8 to 0.1 V at a scan rate of 50 mV s^{-1}.

Electrochemical Scanning Tunneling Microscopy. The FePc/Au(111) surface was characterized under different applied potentials using electrochemical scanning tunneling microscopy (EC-STM). The EC-STM images under different sample potentials were acquired in the same electrochemical cell setup described in the section above. A tungsten tip was electrochemically etched in 2 M sodium hydroxide and coated with nail polish to reduce faradaic currents under electrochemical conditions. The coated W tip was mounted in a STM scanner (Keysight Technology, 5500STM) and brought into tunneling contact with FePc/Au(111). The difference between the sample and tip potentials is defined as the bias (V_{bias}); this parameter and the tip current (I_{tip}) were controlled by a R9 STM controller (RHK Technology).

EC-TERS Experiment. The same EC-STM setup was utilized for EC-TERS experiments. An Ag tip was used in the EC-TERS experiment to generate the highly confined near-field at the tip apex. The Ag tip was electrochemically etched in a 4:1 volume mixture of ethanol and perchloric acid and was insulated using nail polish. A HeNe laser (λ = 632.8 nm, 0.5 mW) was focused on the tip apex using a 50× objective (Olympus, NA = 0.5). The Raman signal was collected by the same objective lens and fiber-coupled to a spectrometer (Princeton Instruments, IsoPlane SCT320). A detailed description of the optical setup and the experimental apparatus is included in the Supporting Information (Figure S1). Electrochemical surface-enhanced Raman spectroscopy (EC-SERS) was also performed to complement the EC-TERS studies, and a detailed experimental procedure is given in the Supporting Information.

RESULTS AND DISCUSSION

A typical EC-STM image of FePc/Au(111) is shown in Figure 1A. The well-ordered FePc adlayer is characterized by a square unit cell with a lattice constant of 1.4 nm, which is consistent with previous results.[59] The catalytic activity of FePc/Au(111) in aerated 0.1 M $HClO_4$ is shown in Figure 1B, where the ORR onset potential is located at approximately 0.7 V and a clear catalytic wave is observed at 0.5 V. The ORR activity of FePc

DOI: 10.1021/jacs.9b07979
J. Am. Chem. Soc. 2019, 141, 15684−15692

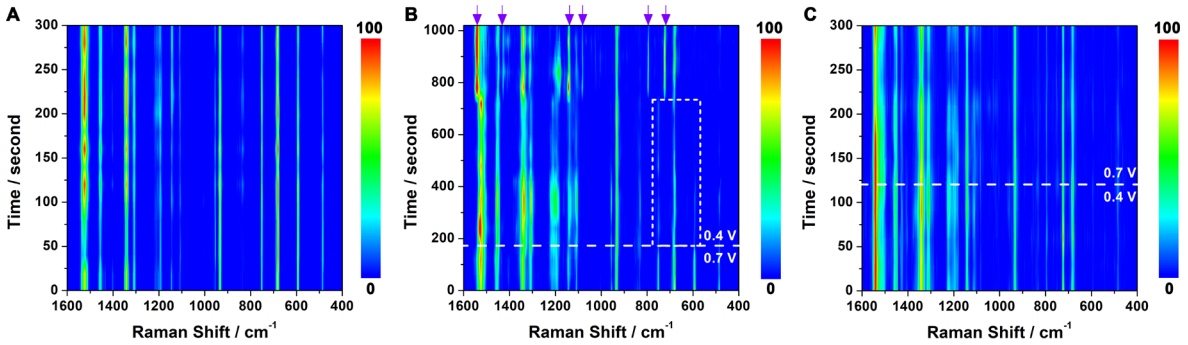

Figure 2. (A) EC-TERS time trace of FePc/Au(111) at 0.7 V in aerated 0.1 M $HClO_4$. (B) EC-TERS time trace of FePc/Au(111) obtained at 0.7 and 0.4 V sample potentials. The time for the potential step from 0.7 to 0.4 V is indicated by the white dashed line. The dashed rectangle highlights the peak attenuation at 593, 682, and 750 cm^{-1}. Purple arrows atop the waterfall plot indicate the location of new Raman peaks. (C) EC-TERS time trace of FePc/Au(111) acquired at 0.4 and 0.7 V sample potentials. The potential step direction is anodic. TERS conditions: Ag tip, λ = 632.8 nm at 0.5 mW, V_{bias} = 0.3 V with I_{tip} = 0.5 nA, and 10 s integration time. All EC-TER spectra are normalized to the perchlorate ion peak at 934 cm^{-1}.

reported here is consistent with previous studies.[57,58,60,61] As expected, the ORR activity of a clean Au(111) surface is lower compared to FePc, with a more negative onset potential and lower ORR current density (Figure 1B). The (111) orientation of the Au single crystal is confirmed using cyclic voltammetry (Figure S2), which rules out the contribution of other crystal orientations to the ORR activity of the Au substrate. Representative EC-TER spectra acquired when the Ag tip is engaged and retracted are shown in Figure 1C. In TERS experiments, when an Ag tip is in the electron tunneling regime with the sample, a plasmonic hot spot can form in the tip−sample junction and locally enhance the Raman intensity of molecules in the junction.[62−64] This situation is represented by the engaged TER spectrum of FePc/Au(111) in Figure 1C. In contrast, the highly localized field is no longer present near the surface when the Ag tip is retracted from the sample surface, which results in a very weak Raman signal as shown by the retracted spectrum (Figure 1C). The Ag tip in the retracted state is between 200 and 300 nm from the surface, and the exact value would depend on the piezo position of the engaged tip prior to retraction. The EC-TER spectrum of FePc/Au(111) agrees with previously reported Raman spectra of this molecule,[65,66] and the peak at 934 cm^{-1} is attributed to perchlorate ions in the supporting electrolyte.[67]

To investigate the effect of ORR catalysis on the chemical structure of FePc, EC-TER spectra are collected during chronoamperometry at different sample potentials. Figure 2A illustrates an EC-TERS time trace of FePc/Au(111) at 0.7 V, prior to the onset of ORR. The EC-TER spectra are normalized to the peak intensity of perchlorate ions at 934 cm^{-1}. The reason for normalizing the EC-TER spectra to the perchlorate peak is to minimize the effect of laser power fluctuations for a fair comparison between the EC-TER spectra. No obvious change in the spectral feature is observed in the EC-TER spectrum of FePc molecules over time other than some fluctuations in the peak intensities. Signal fluctuations are commonly observed in TERS measurements where a single or a few molecules are probed by the plasmonic tip. The observed fluctuations can be attributed to several reasons such as small variation in the excited states,[68] temperature,[69] or changes in the plasmonic hot spot as the Ag tip traverses the FePc/Au(111) surface due to sample thermal drift. Following a potential step to 0.4 V under which the FePc molecules are catalyzing ORR, two important changes to the EC-TER spectrum of FePc are observed in Figure 2B. Immediately after the potential step to 0.4 V, an attenuation to the intensity of peaks at 593, 682, and 751 cm^{-1} is evident (Figure 2B, dashed rectangles). We distinguish this attenuation from intensity fluctuations observed in Figure 2A based on the consideration that the latter affects all peaks in the EC-TER spectrum of FePc, which is a stark contrast to the spectral changes in Figure 2B whereby only peaks at 593, 682, and 751 cm^{-1} are attenuated. The attenuation in these peak intensities can be recovered when the sample potential is quickly switched between 0.7 and 0.4 V as shown in Figure S3. This indicates that the physical or chemical change that causes peak attenuation is reversible. After a potential hold at 0.4 V for 10 min, a significant change to the EC-TER spectrum of FePc occurred as indicated by the formation of new peaks, most notably at 724 and 795 cm^{-1} (Figure 2B, arrows). Simultaneously, the peaks located at 593 and 751 cm^{-1} that are characteristic to FePc disappeared. Moreover, clear spectral changes in the regions centered around 1083, 1142, 1512, and 1542 cm^{-1} suggest that these new vibrational modes can be attributed to a new molecule unlike FePc (vide infra). It should be noted that Au(111) demonstrates minimal ORR activity at 0.4 V (Figure 1B); thus, the majority of catalytic turnover occurs on FePc.

Figure 2C illustrates the EC-TER spectrum of FePc/Au(111) when the sample potential is returned to 0.7 V after a drastic change in the FePc spectrum has occurred. Clearly, the original TER spectrum of FePc obtained prior to ORR (Figure 2A) is not recovered. This observation strongly supports that FePc molecules have undergone irreversible change after an extended polarization at 0.4 V where ORR is occurring. This is in strong contrast compared to the reversible change to the peak intensity as shown in Figure S3. Noteworthy, EC-TERS is a nanoscale probe, and the plasmonic hot spot that enhances Raman scattering is based on a highly localized near-field confined at the tip apex. As a result, the associated EC-TER spectrum reflects the local chemical information. Therefore, the absence of FePc spectral features at 0.7 V in Figure 2C does not imply a complete alteration of all FePc molecules on Au(111). As portrayed in Figure S4, both pristine and altered FePc molecules can be observed at different sample locations on FePc/Au(111) at 0.7 V after ORR catalysis at 0.4 V.

DOI: 10.1021/jacs.9b07979
J. Am. Chem. Soc. 2019, 141, 15684−15692

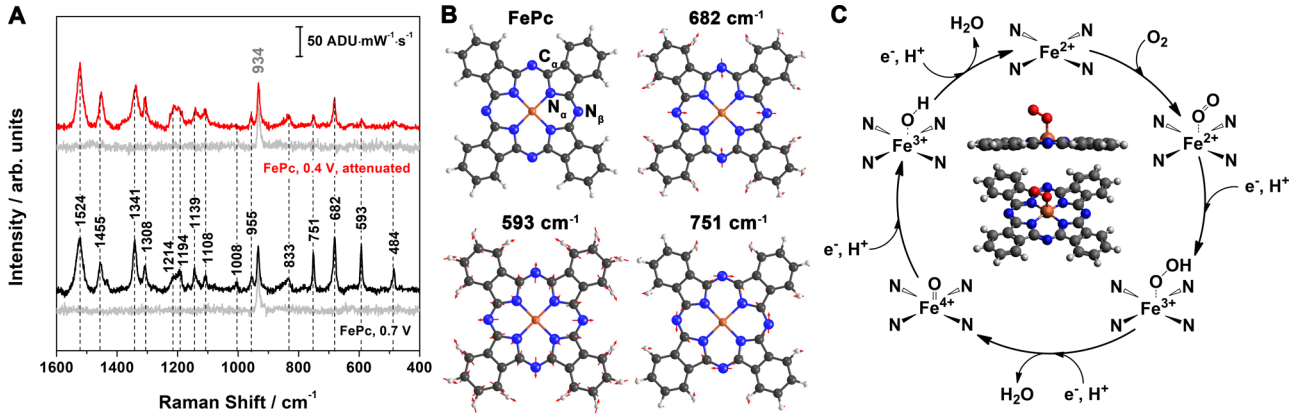

Figure 3. (A) EC-TERS spectra of FePc/Au(111) at 0.7 and 0.4 V in aerated 0.1 M $HClO_4$. The spectrum in red color represents the FePc molecule immediately after the sample potential is set to 0.4 V. The associated tip-retracted spectra are plotted in gray color. (B) Calculated geometry of FePc shown with ball-and-stick models. The white, gray, blue, and orange color atoms represent hydrogen, carbon, nitrogen, and iron, respectively. The red arrows indicate the atomic displacement vectors of the respective FePc vibrations at 594, 682, and 751 cm^{-1}. (C) The proposed ORR catalytic cycle on FePc. The calculated geometry of the FePc−(O_2) adduct is shown in the center of the catalytic cycle. Side-view of the FePc−(O_2) adduct illustrates the displacement of Fe above the macrocycle plane. TERS conditions: Ag tip, λ = 632.8 nm at 0.5 mW, V_{bias} = 0.3 V with I_{tip} = 0.5 nA, and 10 s integration time.

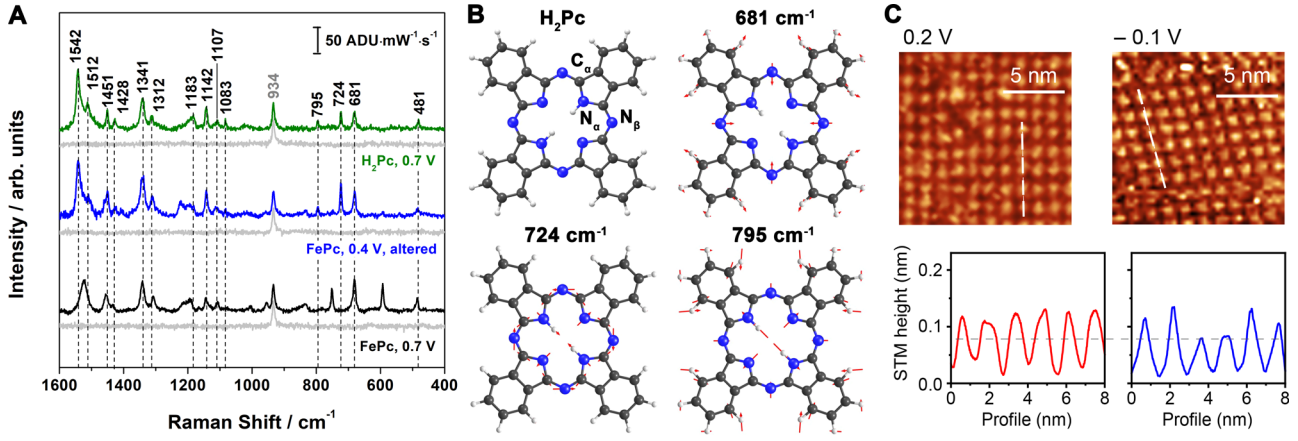

Figure 4. (A) EC-TER spectra of FePc/Au(111) at 0.7 and 0.4 V (black and blue) and H_2Pc at 0.7 V (green) in aerated 0.1 M $HClO_4$. The blue spectrum was obtained after 15 min of potential hold at 0.4 V. The corresponding tip-retracted spectrum is plotted in gray color. (B) Calculated geometry of H_2Pc shown with ball-and-stick models. The white, gray, and blue color atoms represent hydrogen, carbon, and nitrogen, respectively. The red arrows indicate the atomic displacement vectors of the respective H_2Pc vibrations at 681, 724, and 795 cm^{-1}. (C) EC-STM images of FePc/Au(111) at 0.7 and 0.4 V (top panels), and the associated height profiles along the dashed lines shown underneath illustrate two levels of height corrugation. TERS conditions: Ag tip, λ = 632.8 nm at 0.5 mW, V_{bias} = 0.3 V with I_{tip} = 0.5 nA, and 10 s integration time. STM conditions: W tip, V_{bias} = 0.9 V, and I_{tip} = 2 nA.

The EC-TER spectra of different FePc species observed in the chronoamperometry experiments are shown in Figure 3A. To better understand the spectral change of the FePc molecules, vibrational frequency and Raman calculations for a free molecule were performed (Figure S5 and Table S1). The calculated displacement vectors in Figure 3B indicate that a significant component of the peaks at 593, 682, and 751 cm^{-1} is associated with the motion of the α carbon (C_α), isoindole nitrogen (N_α), and bridge nitrogen (N_β), which comprise the core of the FePc molecule. Notably, the $C_\alpha-N_\alpha-C_\alpha$ vibrational motions of the peaks at 593 and 751 cm^{-1} are also kinematically coupled to the Fe−N_α bond stretching. Normal mode analysis of the attenuated peaks suggests that ORR catalysis can have an effect on specific vibrations, particularly those pertinent to the $C_\alpha-N_\alpha-C_\alpha$, $C_\alpha-N_\beta-C_\alpha$, and Fe−$N_\alpha$ groups. To rationalize this, we consider the participation of FePc in the ORR mechanism. During catalysis, the adsorption of O_2 and its subsequent transformation to different reaction intermediates, such as OOH_{ads}, O_{ads}, and OH_{ads}, occur directly at the Fe site (Figure 3C).[70−73] The formation of oxygen-containing adducts bound to the FePc molecule can lead to a nonplanar geometry in which the Fe ion is displaced above the molecular plane of the macrocycle.[6,9,11,12,74,75] The formation of nonplanar FePc during ORR has been observed using in situ X-ray absorption spectroscopy.[6,9,11,74] Using in situ SERS measurements, Melendres et al. have ascribed the attenuation and broadening of FePc Raman peaks under cathodic polarization to a distortion in the molecular geometry (doming) of FePc.[65] Combining the EC-TERS data and normal mode calculations with existing knowledge in the literature, we postulate that the intensity decrease at 593, 682, and 751 cm^{-1} can be related to the formation of nonplanar FePc. Additionally, the FeN_4 sites have been shown to undergo a switching behavior in which the Fe ion can move away or toward the N_4-plane during ORR based on in situ X-ray absorption spectroscopy.[11] This can be

DOI: 10.1021/jacs.9b07979
J. Am. Chem. Soc. 2019, 141, 15684−15692

one explanation for the reversible change in the FePc peak intensities as the sample potential is rapidly switched between 0.7 and 0.4 V (Figure S3). Moreover, no attenuation of the peaks at 593, 682, and 751 cm^{-1} is observed at 0.4 V in N_2-saturated electrolyte, which affirms that the spectral changes observed in EC-TERS are indeed a consequence of ORR catalysis and not simply a result of applied cathodic potentials (Figure S6).

Unlike the reversible spectral changes that occur after short cathodic polarization, an irreversible change of FePc molecule is observed after a potential hold at 0.4 V for 15 min (blue spectrum in Figure 4A). Compared to the TER spectrum acquired at 0.7 V (black spectrum in Figure 4A), the peaks at 593 and 751 cm^{-1} have completely disappeared. Additionally, the appearance of two prominent peaks at 724 and 795 cm^{-1} as well as the spectral changes at around 1083, 1142, 1512, and 1542 cm^{-1} clearly distinguish the altered FePc species from the pristine molecule. Excellent agreement is obtained when the spectrum of the altered FePc species is compared to that of free base phthalocyanine (H_2Pc) (green spectrum in Figure 4A). According to the calculated normal modes of H_2Pc (Figure 4B), the peak at 724 cm^{-1} is related to the rocking of $C_\alpha-N_\alpha-C_\alpha$ and N−H in-plane bending, which are coupled to the overall stretching and deformation of the isoindole groups. The peak at 795 cm^{-1} is ascribed to $C_\alpha-C-N_\beta$ motions and macrocycle ring deformation. Additionally, the highly Raman-active mode at 1524 cm^{-1} is sensitive to the cavity size of the Pc molecule, and the observed red shift of the peak to 1542 cm^{-1} is consistent with a larger cavity size of the H_2Pc molecule.[76] Based on the clear Raman fingerprints of H_2Pc, we conclude that irreversible demetalation of FePc can occur during ORR catalysis. The calculated Raman spectrum of the free H_2Pc molecule is included in the Supporting Information (Figure S7 and Table S2).

The irreversible demetalation of FePc during ORR can be rationalized considering the large degree of molecular distortion and the thermodynamic driving force that favors solvated Fe^{2+} formation, most likely a hexaaquairon(II) complex. One consequence of FePc adopting a nonplanar geometry is an outward displacement of the Fe ion, which leads to an increase in the Fe−N bond length.[6,9,11,75] Moreover, a solvated Fe^{2+} is the thermodynamically stable Fe species under the ORR condition based on the Pourbaix diagram of Fe.[77] Lastly, a smaller Pc cavity is necessary to accommodate the smaller $Fe^{3+/4+}$ ions that can form during ORR, which can induce further ring deformation.[76] Summing these arguments, we believe that ORR catalysis can lead to the release of Fe^{2+} from nonplanar FePc molecules into the electrolyte. Prior to this work, indirect evidence of FePc demetalation based on measurements of Fe content in the electrolyte has been used to infer the occurrence of demetalation.[21,25] However, these studies cannot distinguish whether demetalation proceeds through a direct loss of Fe or by carbon corrosion. The EC-TERS results presented in this study provide unambiguous evidence for the direct demetalation of FePc during ORR. The degraded product of FePc is successfully characterized as H_2Pc in which the macrocyclic structure is retained. This indicates that the demetalation of FePc during ORR proceeds via a direct loss of Fe^{2+} and that carbon corrosion is not the operative mechanism. Through a series of systematic studies at different laser exposure durations, and in the presence and absence of O_2 (Figures S8), we confirmed that FePc demetalation is a result of ORR catalysis and not a result of applying potentials or laser illumination

EC-STM is also used to visualize the change in FePc at different applied potentials. A line profile along the principal axis of the FePc unit cell shows a height corrugation of approximately 1 Å at 0.7 V. Following a potential step to 0.4 V, some molecules in the FePc domain exhibit a lower height corrugation of 0.5 Å. Based on the simulated STM images (Figure S9), H_2Pc is expected to exhibit a lower contrast compared to FePc due to a lower electron density in the Pc cavity. As a result, we attribute the lower contrast features in the EC-STM image of FePc/Au(111) at 0.4 V to the H_2Pc molecules that are formed due to FePc demetalation. Gu et al. have also reported bright and dim features in the EC-STM images of FePc/Au(111) prior to ORR and during catalysis.[59] These authors ascribed the high and low contrast features to the $FePc-O_2$ complexes and O_2-free FePc molecules, respectively. The height corrugation associated with FePc in Figure 4C agrees well with the value obtained by Gu et al.;[59] however, these authors did not report species associated with H_2Pc. According to the EC-TERS results in Figure 2B, the demetalation of FePc does not occur immediately after a potential step to 0.4 V, and not all molecules undergo demetalation. Thus, the absence of low-contrast features in the study by Gu et al. does not contradict our results.

An important consequence of FePc demetalation is the loss of FeN_4 sites and the simultaneous in situ formation of new CN_x sites in H_2Pc (Figure S10). With increasing potential hold time at 0.4 V, the ratio of FeN_4 to CN_x sites on the Au(111) surface is expected to decrease, which provides an opportunity to investigate the ORR activity of FeN_4 and CN_x sites. To study this, the current density and the ORR onset potential of FePc/Au(111) after different potential hold times are monitored (Figure 5). The time-dependent ORR activity of FePc/Au(111) reveals a progressive decrease in the current density and a continuing negative shift of the onset potential. After 15 min of applying potential at 0.4 V, a slight decrease in the ORR activity is observed indicating only a small number of FePc molecules have undergone demetalation. After 60 min, a substantial negative shift in the ORR onset potential by 114 mV and a 26% decrease in the peak current density are observed. We attribute the clear loss in the ORR activity to the demetalation of FePc and an increase in the concentration of in situ formed CN_x sites. Other processes such as FePc diffusion and desorption can also affect the ORR activity; however, they are not the primary cause for the observed performance loss (Figure S11). The decrease in the ORR peak current density can be fitted with an exponential decay function, providing an estimated half-life ($t_{1/2}$) of 51 min for the current loss. This value is of the same order of magnitude compared to the pyrolyzed Fe/N/C catalysts examined by Chenitz et al.[20] The shorter $t_{1/2}$ observed in our study compared to the reported time constants is reasonable since the pyrolyzed Fe/N/C catalysts generally possess greater stability.[78] Combining the electrochemical and the EC-TERS results, the correlation between ORR activity loss and FePc demetalation suggests that the CN_x moieties which remain on the H_2Pc molecules after demetalation have inferior ORR activity compared to the FeN_4 site in FePc.

CONCLUSIONS

In conclusion, a reversible change followed by an irreversible degradation of FePc has been observed during ORR catalysis

DOI: 10.1021/jacs.9b07979
J. Am. Chem. Soc. 2019, 141, 15684−15692

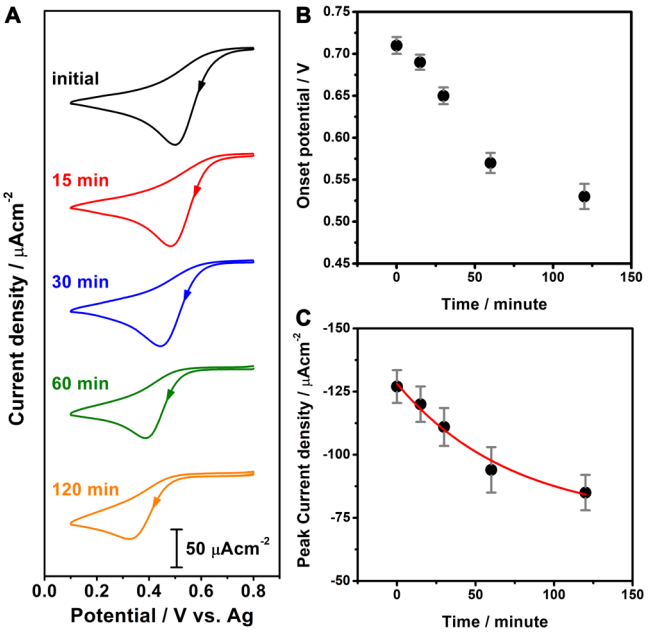

Figure 5. (A) CVs of FePc/Au(111) in aerated 0.1 M $HClO_4$ at a scan rate of 50 mVs^{-1} showing the initial ORR activity (black) and the activity after a potential step to 0.4 V for different time. (B) Time-dependent ORR onset potential of FePc/Au(111). (C) Time-dependent ORR peak current density at 0.4 V. The red line represents an exponential fit to the current decay. The potential and current density values plotted are the average of five different measurements.

using EC-TERS and EC-STM. The combination of EC-TERS and DFT calculations suggested the formation of a nonplanar geometry of FePc during ORR catalysis at 0.4 V. Under extended cathodic polarization, we have reported for the first time clear evidence that support the direct demetalation of FePc based on unambiguous changes in the EC-TER spectra. Additionally, the product of FePc degradation has been identified as H_2Pc, which clarifies that the degradation mechanism of FePc involves a direct demetalation process. Moreover, an exponential decay in the ORR activity of FePc was observed with increase cathodic polarization time, which can be correlated with a progressive demetalation of FePc and the in situ formation of CN_x sites. Combining the EC-TERS, EC-STM, and time-dependent electrochemical activity measurements, it is concluded that the Fe ion is essential for the activity of FePc and a direct demetalation of the macrocyle is the dominant mechanism in catalyst degradation. In a broader scheme, our study demonstrated a successful implementation of EC-TERS in understanding the chemical changes of a model catalyst during an electrochemical reaction.

■ ASSOCIATED CONTENT

Supporting Information

The Supporting Information is available free of charge on the ACS Publications website at DOI: 10.1021/jacs.9b07979.

Details for experimental setup, EC-SERS measurements, and stimulation details; cyclic voltammogram of Au(111); EC-TERS of FePc/Au(111) showing reversible spectral change; EC-TERS of FePc/Au(111) at different sample locations; calculated Raman spectrum of FePc and H_2Pc; EC-SERS of FePc in aerated and N_2-saturated electrolyte; schematic illustration of FePc demetalation and H_2Pc formation; simulated STM of FePc/Au(111) and H_2Pc/Au(111); ORR performance of FePc/Au(111) at different potential hold times and exponent fit to current decay (PDF)

■ AUTHOR INFORMATION

Corresponding Authors

*vanduyne@northwestern.edu
*g-schatz@northwestern.edu

ORCID

Zhu Chen: 0000-0001-5889-5415
Song Jiang: 0000-0002-2223-8517
Gyeongwon Kang: 0000-0002-8219-2717
Duc Nguyen: 0000-0002-6591-6429
George C. Schatz: 0000-0001-5837-4740
Richard P. Van Duyne: 0000-0001-8861-2228

Notes

The authors declare no competing financial interest.

■ ACKNOWLEDGMENTS

The authors acknowledge financial support from the Air Force Office of Scientific Research MURI (FA9550-14-1-0003). Z.C. acknowledges support from the National Science Foundation under grant no. CHE-1807278. G.K., D.N., G.C.S., and R.P.V.D. acknowledge support from the National Science Foundation Center for Chemical Innovation dedicated to Chemistry at the Space-Time Limit (CaSTL) Grant CHE-1414466. G.K. and G.C.S. acknowledge support from Northwestern University Information Technology (NUIT) team and the Center for Nanoscale Materials (CNM) at Argonne National Laboratory for the computational resources. The authors thank Dr. Allen J. Bard, Dr. Henry White, Dr. Martin Edwards, and Dr. Katherine A. Willets for helpful discussions.

■ REFERENCES

(1) Banham, D.; Ye, S. Y. Current status and future development of catalyst materials and catalyst layers for proton exchange membrane fuel cells: an industrial perspective. *ACS Energy Lett.* **2017**, *2*, 629−638.

(2) Kongkanand, A.; Mathias, M. F. The priority and challenge of high-power performance of low-platinum proton-exchange membrane fuel cells. *J. Phys. Chem. Lett.* **2016**, *7*, 1127−1137.

(3) Thompson, S. T.; James, B. D.; Huya-Kouadio, J. M.; Houchins, C.; DeSantis, D. A.; Ahluwalia, R.; Wilson, A. R.; Kleen, G.; Papageorgopoulos, D. Direct hydrogen fuel cell electric vehicle cost analysis: System and high-volume manufacturing description, validation, and outlook. *J. Power Sources* **2018**, *399*, 304−313.

(4) Chung, H. T.; Cullen, D. A.; Higgins, D.; Sneed, B. T.; Holby, E. F.; More, K. L.; Zelenay, P. Direct atomic-level insight into the active sites of a high-performance PGM-free ORR catalyst. *Science* **2017**, *357*, 479−483.

(5) Lefevre, M.; Proietti, E.; Jaouen, F.; Dodelet, J. P. Iron-based catalysts with improved oxygen reduction activity in polymer electrolyte fuel cells. *Science* **2009**, *324*, 71−74.

(6) Li, J. K.; Ghoshal, S.; Liang, W. T.; Sougrati, M. T.; Jaouen, F.; Halevi, B.; McKinney, S.; McCool, G.; Ma, C. R.; Yuan, X. X.; Ma, Z. F.; Mukerjee, S.; Jia, Q. Y. Structural and mechanistic basis for the high activity of Fe-N-C catalysts toward oxygen reduction. *Energy Environ. Sci.* **2016**, *9*, 2418−2432.

(7) Strickland, K.; Miner, E.; Jia, Q. Y.; Tylus, U.; Ramaswamy, N.; Liang, W. T.; Sougrati, M. T.; Jaouen, F.; Mukerjee, S. Highly active oxygen reduction non-platinum group metal electrocatalyst without direct metal-nitrogen coordination. *Nat. Commun.* **2015**, *6*, 7343.

DOI: 10.1021/jacs.9b07979
J. Am. Chem. Soc. 2019, 141, 15684−15692

(8) Wu, G.; More, K. L.; Johnston, C. M.; Zelenay, P. High-performance electrocatalysts for oxygen reduction derived from polyaniline, iron, and cobalt. *Science* **2011**, *332*, 443−447.
(9) Zitolo, A.; Goellner, V.; Armel, V.; Sougrati, M. T.; Mineva, T.; Stievano, L.; Fonda, E.; Jaouen, F. Identification of catalytic sites for oxygen reduction in iron- and nitrogen-doped graphene materials. *Nat. Mater.* **2015**, *14*, 937−942.
(10) Armel, V.; Hindocha, S.; Salles, F.; Bennett, S.; Jones, D.; Jaouen, F. Structural descriptors of zeolitic-imidazolate frameworks are keys to the activity of Fe-N-C catalysts. *J. Am. Chem. Soc.* **2017**, *139*, 453−464.
(11) Jia, Q.; Ramaswamy, N.; Hafiz, H.; Tylus, U.; Strickland, K.; Wu, G.; Barbiellini, B.; Bansil, A.; Holby, E. F.; Zelenay, P.; Mukerjee, S. Experimental observation of redox-induced Fe-N switching behavior as a determinant role for oxygen reduction activity. *ACS Nano* **2015**, *9*, 12496−12505.
(12) Kramm, U. I.; Herranz, J.; Larouche, N.; Arruda, T. M.; Lefevre, M.; Jaouen, F.; Bogdanoff, P.; Fiechter, S.; Abs-Wurmbach, I.; Mukerjee, S.; Dodelet, J. P. Structure of the catalytic sites in Fe/N/C-catalysts for O-2-reduction in PEM fuel cells. *Phys. Chem. Chem. Phys.* **2012**, *14*, 11673−11688.
(13) Kramm, U. I.; Lefevre, M.; Larouche, N.; Schmeisser, D.; Dodelet, J. P. Correlations between mass activity and physicochemical properties of Fe/N/C catalysts for the ORR in PEM fuel cell via ^{57}Fe Mössbauer spectroscopy and other techniques. *J. Am. Chem. Soc.* **2014**, *136*, 978−985.
(14) Tylus, U.; Jia, Q. Y.; Strickland, K.; Ramaswamy, N.; Serov, A.; Atanassov, P.; Mukerjee, S. Elucidating oxygen reduction active sites in pyrolyzed metal-nitrogen coordinated non-precious-metal electrocatalyst systems. *J. Phys. Chem. C* **2014**, *118*, 8999−9008.
(15) Ding, W.; Wei, Z. D.; Chen, S. G.; Qi, X. Q.; Yang, T.; Hu, J. S.; Wang, D.; Wan, L. J.; Alvi, S. F.; Li, L. Space-confinement-induced synthesis of pyridinic- and pyrrolic-nitrogen-doped graphene for the catalysis of oxygen reduction. *Angew. Chem., Int. Ed.* **2013**, *52*, 11755−11759.
(16) Dodelet, J. P.; Chenitz, R.; Yang, L. J.; Lefevre, M. A new catalytic site for the electroreduction of oxygen? *ChemCatChem* **2014**, *6*, 1866−1867.
(17) Guo, D. H.; Shibuya, R.; Akiba, C.; Saji, S.; Kondo, T.; Nakamura, J. Active sites of nitrogen-doped carbon materials for oxygen reduction reaction clarified using model catalysts. *Science* **2016**, *351*, 361−365.
(18) Baker, R.; Wilkinson, D. P.; Zhang, J. J. Electrocatalytic activity and stability of substituted iron phthalocyanines towards oxygen reduction evaluated at different temperatures. *Electrochim. Acta* **2008**, *53*, 6906−6919.
(19) Baranton, S.; Coutanceau, C.; Roux, C.; Hahn, F.; Leger, J. M. Oxygen reduction reaction in acid medium at iron phthalocyanine dispersed on high surface area carbon substrate: tolerance to methanol, stability and kinetics. *J. Electroanal. Chem.* **2005**, *577*, 223−234.
(20) Chenitz, R.; Kramm, U. I.; Lefevre, M.; Glibin, V.; Zhang, G. X.; Sun, S. H.; Dodelet, J. P. A specific demetalation of Fe-N_4 catalytic sites in the micropores of NC_Ar + NH_3 is at the origin of the initial activity loss of the highly active Fe/N/C catalyst used for the reduction of oxygen in PEM fuel cells. *Energy Environ. Sci.* **2018**, *11*, 365−382.
(21) Choi, C. H.; Baldizzone, C.; Polymeros, G.; Pizzutilo, E.; Kasian, O.; Schuppert, A. K.; Sahraie, N. R.; Sougrati, M. T.; Mayrhofer, K. J. J.; Jaouen, F. Minimizing operando demetallation of Fe-N-C electrocatalysts in acidic medium. *ACS Catal.* **2016**, *6*, 3136−3146.
(22) Goellner, V.; Baldizzone, C.; Schuppert, A.; Sougrati, M. T.; Mayrhofer, K.; Jaouen, F. Degradation of Fe/N/C catalysts upon high polarization in acid medium. *Phys. Chem. Chem. Phys.* **2014**, *16*, 18454−18462.
(23) Kumar, K.; Gairola, P.; Lions, M.; Ranjbar-Sahraie, N.; Mermoux, M.; Dubau, L.; Zitolo, A.; Jaouen, F.; Maillard, F. Physical and chemical considerations for improving catalytic activity and stability of non-precious-metal oxygen reduction reaction catalysts. *ACS Catal.* **2018**, *8*, 11264−11276.
(24) Li, W. M.; Yu, A. P.; Higgins, D. C.; Llanos, B. G.; Chen, Z. W. Biologically inspired highly durable iron phthalocyanine catalysts for oxygen reduction reaction in polymer electrolyte membrane fuel cells. *J. Am. Chem. Soc.* **2010**, *132*, 17056−17058.
(25) Choi, C. H.; Baldizzone, C.; Grote, J. P.; Schuppert, A. K.; Jaouen, F.; Mayrhofer, K. J. J. Stability of Fe-N-C catalysts in acidic medium studied by operando spectroscopy. *Angew. Chem., Int. Ed.* **2015**, *54*, 12753−12757.
(26) Choi, C. H.; Lim, H. K.; Chung, M. W.; Chon, G.; Sahraie, N. R.; Altin, A.; Sougrati, M. T.; Stievano, L.; Oh, H. S.; Park, E. S.; Luo, F.; Strasser, P.; Drazic, G.; Mayrhofer, K. J. J.; Kim, H.; Jaouen, F. The Achilles' heel of iron-based catalysts during oxygen reduction in an acidic medium. *Energy Environ. Sci.* **2018**, *11*, 3176−3182.
(27) Goellner, V.; Armel, V.; Zitolo, A.; Fonda, E.; Jaouen, F. Degradation by hydrogen peroxide of metal-nitrogen-carbon catalysts for oxygen reduction. *J. Electrochem. Soc.* **2015**, *162*, H403−H414.
(28) Zhang, G. X.; Chenitz, R.; Lefevre, M.; Sun, S.; Dodelet, J. P. Is iron involved in the lack of stability of Fe/N/C electrocatalysts used to reduce oxygen at the cathode of PEM fuel cells? *Nano Energy* **2016**, *29*, 111−125.
(29) Meier, H.; Tschirwitz, U.; Zimmerhackl, E.; Albrecht, W.; Zeitler, G. Application of radioisotope techniques for the study of phthalocyanine catalyzed electrochemical processes in fuel cells. *J. Phys. Chem.* **1977**, *81*, 712−718.
(30) Ramaswamy, N.; Tylus, U.; Jia, Q. Y.; Mukerjee, S. Activity descriptor identification for oxygen reduction on nonprecious electrocatalysts: linking surface science to coordination chemistry. *J. Am. Chem. Soc.* **2013**, *135*, 15443−15449.
(31) Kramm, U. I.; Lefevre, M.; Bogdanoff, P.; Schmeisser, D.; Dodelet, J. P. Analyzing structural changes of Fe-N-C cathode catalysts in PEM fuel cell by Mössbauer spectroscopy of complete membrane electrode assemblies. *J. Phys. Chem. Lett.* **2014**, *5*, 3750−3756.
(32) Holby, E. F.; Wu, G.; Zelenay, P.; Taylor, C. D. Structure of Fe-N_x-C defects in oxygen reduction reaction catalysts from first-principles modeling. *J. Phys. Chem. C* **2014**, *118*, 14388−14393.
(33) Szakacs, C. E.; Lefevre, M.; Kramm, U. I.; Dodelet, J. P.; Vidal, F. A density functional theory study of catalytic sites for oxygen reduction in Fe/N/C catalysts used in H_2/O_2 fuel cells. *Phys. Chem. Chem. Phys.* **2014**, *16*, 13654−13661.
(34) Kim, H.; Kosuda, K. M.; Van Duyne, R. P.; Stair, P. C. Resonance Raman and surface- and tip-enhanced Raman spectroscopy methods to study solid catalysts and heterogeneous catalytic reactions. *Chem. Soc. Rev.* **2010**, *39*, 4820−4844.
(35) Hartman, T.; Wondergem, C. S.; Kumar, N.; van den Berg, A.; Weckhuysen, B. M. Surface- and tip-enhanced Raman spectroscopy in catalysis. *J. Phys. Chem. Lett.* **2016**, *7*, 1570−1584.
(36) Pfisterer, J. H. K.; Domke, K. F. Unfolding the versatile potential of EC-TERS for electrocatalysis. *Curr. Opin. Electrochem.* **2018**, *8*, 96−102.
(37) Zeng, Z. C.; Huang, S. C.; Wu, D. Y.; Meng, L. Y.; Li, M. H.; Huang, T. X.; Zhong, J. H.; Wang, X.; Yang, Z. L.; Ren, B. Electrochemical tip-enhanced Raman spectroscopy. *J. Am. Chem. Soc.* **2015**, *137*, 11928−11931.
(38) Zaleski, S.; Wilson, A. J.; Mattei, M.; Chen, X.; Goubert, G.; Cardinal, M. F.; Willets, K. A.; Van Duyne, R. P. Investigating nanoscale electrochemistry with surface- and tip-enhanced Raman spectroscopy. *Acc. Chem. Res.* **2016**, *49*, 2023−2030.
(39) Zhang, R.; Zhang, Y.; Dong, Z. C.; Jiang, S.; Zhang, C.; Chen, L. G.; Zhang, L.; Liao, Y.; Aizpurua, J.; Luo, Y.; Yang, J. L.; Hou, J. G. Chemical mapping of a single molecule by plasmon-enhanced Raman scattering. *Nature* **2013**, *498*, 82−86.
(40) Jiang, S.; Zhang, Y.; Zhang, R.; Hu, C. R.; Liao, M. H.; Luo, Y.; Yang, J. L.; Dong, Z. C.; Hou, J. G. Distinguishing adjacent molecules on a surface using plasmon-enhanced Raman scattering. *Nat. Nanotechnol.* **2015**, *10*, 865−869.

DOI: 10.1021/jacs.9b07979
J. Am. Chem. Soc. 2019, 141, 15684−15692

(41) Lee, J. H.; Tallarida, N.; Chen, X.; Liu, P. C.; Jensen, L.; Apkarian, V. A. Tip-enhanced Raman spectromicroscopy of Co(II)-tetraphenylporphyrin on Au(111): toward the chemists' microscope. *ACS Nano* **2017**, *11*, 11466−11474.
(42) Nguyen, D.; Kang, G.; Chiang, N. H.; Chen, X.; Seideman, T.; Hersam, M. C.; Schatz, G. C.; Van Duyne, R. P. Probing molecular-scale catalytic interactions between oxygen and cobalt phthalocyanine using tip-enhanced Raman spectroscopy. *J. Am. Chem. Soc.* **2018**, *140*, 5948−5954.
(43) van Schrojenstein Lantman, E. M.; Deckert-Gaudig, T.; Mank, A. J. G.; Deckert, V.; Weckhuysen, B. M. Catalytic processes monitored at the nanoscale with tip-enhanced Raman spectroscopy. *Nat. Nanotechnol.* **2012**, *7*, 583−586.
(44) Szczerbinski, J.; Gyr, L.; Kaeslin, J.; Zenobi, R. Plasmon-driven photocatalysis leads to products known from E-beam and X-ray-induced surface chemistry. *Nano Lett.* **2018**, *18*, 6740−6749.
(45) Zheng, L. Q.; Wang, X.; Shao, F.; Hegner, M.; Zenobi, R. Nanoscale chemical imaging of reversible photoisomerization of an azobenzene-thiol self-assembled monolayer by tip-enhanced Raman spectroscopy. *Angew. Chem., Int. Ed.* **2018**, *57*, 1025−1029.
(46) Su, H. S.; Zhang, X. G.; Sun, J. J.; Jin, X.; Wu, D. Y.; Lian, X. B.; Zhong, J. H.; Ren, B. Real-space observation of atomic site-specific electronic properties of a Pt nanoisland/Au(111) bimetallic surface by tip-enhanced Raman spectroscopy. *Angew. Chem., Int. Ed.* **2018**, *57*, 13177−13181.
(47) Rahaman, M.; Rodriguez, R. D.; Plechinger, G.; Moras, S.; Schuller, C.; Korn, T.; Zahn, D. R. T. Highly localized strain in a MoS_2/Au heterostructure revealed by tip-enhanced Raman spectroscopy. *Nano Lett.* **2017**, *17*, 6027−6033.
(48) Shao, F.; Dai, W. Y.; Zhang, Y.; Zhang, W.; Schluter, A. D.; Zenobi, R. Chemical mapping of nanodefects within 2D covalent monolayers by tip-enhanced Raman spectroscopy. *ACS Nano* **2018**, *12*, 5021−5029.
(49) Kurouski, D.; Mattei, M.; Van Duyne, R. P. Probing redox reactions at the nanoscale with electrochemical tip-enhanced Raman spectroscopy. *Nano Lett.* **2015**, *15*, 7956−7962.
(50) Mattei, M.; Kang, G.; Goubert, G.; Chulhai, D. V.; Schatz, G. C.; Jensen, L.; Van Duyne, R. P. Tip-enhanced Raman voltammetry: coverage dependence and quantitative modeling. *Nano Lett.* **2017**, *17*, 590−596.
(51) Sabanes, N. M.; Ohto, T.; Andrienko, D.; Nagata, Y.; Domke, K. F. Electrochemical TERS elucidates potential-induced molecular reorientation of adenine/Au(111). *Angew. Chem., Int. Ed.* **2017**, *56*, 9796−9801.
(52) Chen, X.; Brasiliense, V.; Van Duyne, R. P. Operando observation of molecular-scale manipulation using electrochemical tip-enhanced Raman spectroscopy. *J. Phys. Chem. C* **2018**, *122*, 24329−24333.
(53) Goubert, G.; Chen, X.; Jiang, S.; Van Duyne, R. P. In situ electrochemical tip-enhanced Raman spectroscopy with a chemically modified tip. *J. Phys. Chem. Lett.* **2018**, *9*, 3825−3828.
(54) Jiang, S.; Chen, Z.; Chen, X.; Nguyen, D.; Mattei, M.; Goubert, G.; Van Duyne, R. P. Investigation of cobalt phthalocyanine at the solid/liquid interface by electrochemical tip-enhanced Raman spectroscopy. *J. Phys. Chem. C* **2019**, *123*, 9852−9859.
(55) Kang, G.; Yang, M. W.; Mattei, M. S.; Schatz, G. C.; Van Duyne, R. P. *In situ* nanoscale redox mapping using tip-enhanced Raman spectroscopy. *Nano Lett.* **2019**, *19*, 2106−2113.
(56) Zagal, J.; Bindra, P.; Yeager, E. A mechanistic study of O_2 reduction on water-soluble phthalocyanines adsorbed on graphite-electrodes. *J. Electrochem. Soc.* **1980**, *127*, 1506−1517.
(57) Tanaka, A. A.; Fierro, C.; Scherson, D.; Yaeger, E. B. Electrocatalytic aspects of iron phthalocyanine and its μ-oxo derivatives dispersed on high surface-area carbon. *J. Phys. Chem.* **1987**, *91*, 3799−3807.
(58) Zagal, J.; Paez, M.; Tanaka, A. A.; Dossantos, J. R.; Linkous, C. A. Electrocatalytic activity of metal phthalocyanines for oxygen reduction. *J. Electroanal. Chem.* **1992**, *339*, 13−30.
(59) Gu, J. Y.; Cai, Z. F.; Wang, D.; Wan, L. J. Single-molecule imaging of iron-phthalocyanine-catalyzed oxygen reduction reaction by *in situ* scanning tunneling microscopy. *ACS Nano* **2016**, *10*, 8746−8750.
(60) Van Den Brink, F.; Visscher, W.; Barendrecht, E. Electrocatalysis of cathodic oxygen reduction by metal phthalocyanines: Part IV. Iron phthalocyanine as electrocatalyst: mechanism. *J. Electroanal. Chem. Interfacial Electrochem.* **1984**, *175*, 279−289.
(61) Van Den Brink, F.; Visscher, W.; Barendrecht, E. Electrocatalysis of cathodic oxygen reduction by metal phthalocyanines: Part III. Iron phthalocyanine as electrocatalyst: experimental part. *J. Electroanal. Chem. Interfacial Electrochem.* **1984**, *172*, 301−325.
(62) Pettinger, B.; Schambach, P.; Villagomez, C. J.; Scott, N. Tip-enhanced Raman spectroscopy: near-fields acting on a few molecules. *Annu. Rev. Phys. Chem.* **2012**, *63*, 379−399.
(63) Richard-Lacroix, M.; Zhang, Y.; Dong, Z. C.; Deckert, V. Mastering high resolution tip-enhanced Raman spectroscopy: towards a shift of perception. *Chem. Soc. Rev.* **2017**, *46*, 3922−3944.
(64) Pozzi, E. K.; Goubert, G.; Chiang, N. H.; Jiang, N.; Chapman, C. T.; McAnally, M. O.; Henry, A. I.; Seideman, T.; Schatz, G. C.; Hersam, M. C.; Van Duyne, R. P. Ultrahigh-vacuum tip-enhanced Raman spectroscopy. *Chem. Rev.* **2017**, *117*, 4961−4982.
(65) Melendres, C. A.; Rios, C. B.; Feng, X.; McMasters, R. In situ laser Raman spectra of iron phthalocyanine adsorbed on copper and gold electrodes. *J. Phys. Chem.* **1983**, *87*, 3526−3531.
(66) Corio, P.; Rubim, J. C.; Aroca, R. Contribution of the Herzberg−Teller mechanism to the surface-enhanced Raman scattering of iron phthalocyanine adsorbed on a silver electrode. *Langmuir* **1998**, *14*, 4162−4168.
(67) Ruan, C. M.; Wang, W.; Gu, A. H. Surface-enhanced Raman scattering for perchlorate detection using cystamine-modified gold nanoparticles. *Anal. Chim. Acta* **2006**, *567*, 114−120.
(68) Sonntag, M. D.; Chulhai, D.; Seideman, T.; Jensen, L.; Van Duyne, R. P. The origin of relative intensity fluctuations in single-molecule tip-enhanced Raman spectroscopy. *J. Am. Chem. Soc.* **2013**, *135*, 17187−17192.
(69) Park, K. D.; Muller, E. A.; Kravtsov, V.; Sass, P. M.; Dreyer, J.; Atkin, J. M.; Raschke, M. B. Variable-temperature tip-enhanced Raman spectroscopy of single-molecule fluctuations and dynamics. *Nano Lett.* **2016**, *16*, 479−487.
(70) Chen, R. R.; Li, H. X.; Chu, D.; Wang, G. F. Unraveling oxygen reduction reaction mechanisms on carbon-supported Fe-phthalocyanine and Co-phthalocyanine catalysts in alkaline solutions. *J. Phys. Chem. C* **2009**, *113*, 20689−20697.
(71) Sun, S. R.; Jiang, N.; Xia, D. G. Density functional theory study of the oxygen reduction reaction on metalloporphyrins and metallophthalocyanines. *J. Phys. Chem. C* **2011**, *115*, 9511−9517.
(72) He, H.; Lei, Y. K.; Xiao, C.; Chu, D. R.; Chen, R. R.; Wang, G. F. Molecular and electronic structures of transition-metal macrocyclic complexes as related to catalyzing oxygen reduction reactions: a density functional theory study. *J. Phys. Chem. C* **2012**, *116*, 16038−16046.
(73) Wang, Y.; Yuan, H.; Li, Y. F.; Chen, Z. F. Two-dimensional iron-phthalocyanine (Fe-Pc) monolayer as a promising single-atom-catalyst for oxygen reduction reaction: a computational study. *Nanoscale* **2015**, *7*, 11633−11641.
(74) Stefan, I. C.; Mo, Y.; Ha, S. Y.; Kim, S.; Scherson, D. A. *In situ* Fe K-Edge X-ray absorption fine structure of a nitrosyl adduct of iron phthalocyanine irreversibly adsorbed on a high area carbon electrode in an acidic electrolyte. *Inorg. Chem.* **2003**, *42*, 4316−4321.
(75) Ferrandon, M.; Wang, X. P.; Kropf, A. J.; Myers, D. J.; Wu, G.; Johnston, C. M.; Zelenay, P. Stability of iron species in heat-treated polyaniline-iron-carbon polymer electrolyte fuel cell cathode catalysts. *Electrochim. Acta* **2013**, *110*, 282−291.
(76) Tackley, D. R.; Dent, G.; Smith, W. E. Phthalocyanines: structure and vibrations. *Phys. Chem. Chem. Phys.* **2001**, *3*, 1419−1426.

DOI: 10.1021/jacs.9b07979
J. Am. Chem. Soc. 2019, 141, 15684−15692

(77) Pesterfield, L. L.; Maddox, J. B.; Crocker, M. S.; Schweitzer, G. K. Pourbaix (E-pH-M) diagrams in three dimensions. *J. Chem. Educ.* **2012**, *89*, 891−899.
(78) Shao, Y.; Dodelet, J. P.; Wu, G.; Zelenay, P. J. A. M. PGM-free cathode catalysts for PEM fuel cells: A mini-review on stability challenges. *Adv. Mater.* **2019**, *31*, 1807615.

DOI: 10.1021/jacs.9b07979
J. Am. Chem. Soc. 2019, 141, 15684−15692